The dependence on structure of the projected vibrational density of states of various phases of ice as calculated by *ab initio* methods



2001 J. Phys.: Condens. Matter 13 9207

(http://iopscience.iop.org/0953-8984/13/41/312)

INSTITUTE OF PHYSICS PUBLISHING JOURNAL OF PHYSICS: CONDENSED MATTER

J. Phys.: Condens. Matter **13** (2001) 9207–9229 PII: S0953-8984(01)17946-4

# The dependence on structure of the projected vibrational density of states of various phases of ice as calculated by *ab initio* methods

**S Jenkins and I Morrison**[1]

Joule Physics Laboratory, Institute for Materials Research, University of Salford, Salford, M5 4WT, UK

E-mail: S.Jenkins@physics.org and I.Morrison@salford.ac.uk

Received 11 October 2000, in final form 8 August 2001
Published 28 September 2001
Online at stacks.iop.org/JPhysCM/13/9207

**Abstract**

We determine the structural data of seven of the polymorphs of ice (ice Ih, ice Ic, ice IX, ice II, ice VI, ice VII and ice VIII) from *ab initio* calculations. The dynamical properties have been analysed within the harmonic approximation via a finite-difference evaluation of dynamical matrices from atomic forces. Supercells are used to model the various ordered and disordered phases considered. Calculations are done at zero pressure in order to compare directly with neutron scattering studies performed on recovered phases. The normal modes are resolved into projections chosen to display their intra- and inter-molecular character. Further projections are performed for ice VI, ice VII and ice VIII to probe the interactions between sub-lattices. Trends in the dynamical results are discussed in terms of changes in the structural complexity of the various phases considered.

## 1. Introduction

Experimental techniques including inelastic neutron scattering, infrared spectroscopy and Raman spectroscopy enable excitations of the crystal structure in condensed matter to be directly measured through a wide range of energies and hence obtain information on the microscopic nature of the bonding. The spectra obtained by these methods applied to the ice phases considered in this study are complicated and difficult to interpret [1] due to both the large ranges of geometrical data and the coexistence of covalent and hydrogen bonding. In such systems *ab initio* simulation of the lattice vibrations provides a direct method for determining the microscopic nature of vibrational modes that characterize different regions of the observed spectra, and is an invaluable tool in the interpretation of these spectra.

[1] Author to whom corresspondence should be addressed.

  

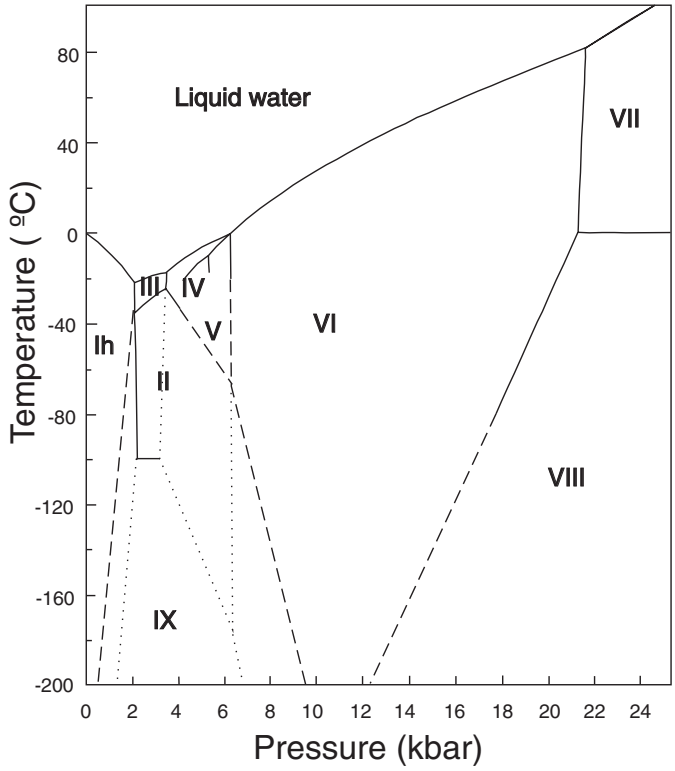


**Figure 1.** The experimental water–ice phase diagram [1].

Here we present a comprehensive study of the structure and dynamical properties of ice across its phase diagram via *ab initio* structural and lattice dynamics simulations. We will present the data in such a way as to highlight trends in the different structures as we move across the phase diagram (see figure 1). In particular we make comparison with dynamical spectra as measured by incoherent inelastic neutron scattering (IINS) studies [2–5]. All of the ice phases considered in this study are comprised of recognizable water molecules and obey the Bernal–Fowler ice rules [6] in that only one hydrogen atom exists between each oxygen nearest neighbour pair forming a covalent bond with one oxygen and a hydrogen bond with the other. Each oxygen atom is coordinated by two covalent bonds and two hydrogen bonds. The near-perfect tetrahedral local geometry of bonding in the low-density phases (ice Ic and ice Ih) is lost in the intermediate density phases (ice IX, ice II and ice VI) and then re-formed in the high-pressure phases (ice VII and ice VIII). The intermediate-pressure phases of ice possess rather non-cylindrical hydrogen bonds, i.e. the hydrogen atom is very non-collinear with the two oxygen atoms at either end of the bonds. In order to explain the origin of features in the vibrational density of states in terms of geometry the projected density of states (PDOS) is used. Here the vibrational density of states is weighted by the projection of eigenvectors onto translational and rotational rigid molecule modes and the normal modes of the water molecules, full details of which are given in section 4.2. Features in the projected vibrational density of states reflect the differences in geometry between phases. Both the low- and high-pressure phases have near-cylindrical hydrogen bonds and, as we show, differences in the spectra between these phases arise mainly from differences in the hydrogen bonded and non-hydrogen bonded oxygen–oxygen separations.

Previous *ab initio* studies have concentrated on specific regions of the phase diagram. The goals of these studies have been diverse: to study the cooperative effects of the interactions between water molecules [7], to explain bond lengths [8], OH vibrational frequencies [9] or the quadrapole coupling constants [10]. Most of these studies have used water clusters of various sizes, with or without the long-range electrostatic interactions being accommodated. Studies on ice VIII have been undertaken using *ab initio* periodic Hartee–Fock calculations [11] and using Carr–Parinello molecular dynamics [12].

The structure of this paper is as follows: in section 2 we briefly outline the geometry of the ice phases and in section 3 we describe the computational methods used throughout the study. In section 4 we present the results, including the predicted structural parameters and vibrational density of states. As mentioned above, the latter are further analysed by projection of the calculated modes onto 'pure' intra-molecular modes and rigid molecule inter-molecular modes to evaluate the PDOS. We present a discussion of trends and links between structural parameters and the PDOS in section 5 and compare with the experiment. Finally we set out our conclusions in section 6.

## 2. Geometry of the various ice structures

The structures of the phases considered in this study are described in detail in [13, 14]. The principal features of the structures and the unit cells used in this study are described here.

Several of the ice phases can be described as near-tetrahedrally coordinated structures (ice Ic, ice Ih, ice VII and ice VIII). In these structures each water molecule is tetrahedrally coordinated by hydrogen bonds to four other molecules. Hydrogen bonds can be labelled according to the relative orientation of the two molecules involved in making the bond. Figure 2 describes the four possible local arrangements of the hydrogen bond, which we label A, B, C and D. Several phases (ice Ic, ice Ih and ice VII) are said to be proton-disordered, i.e. the orientations of the water molecules at each lattice site are disordered. Proton-disordered phases are modelled by a periodic supercell approach. Here representative samples of all possible proton arrangements in a particular supercell are used in the calculations. If and only if one proton arrangement is preferred is the phase considered to be proton-ordered.

Ice Ih can contain A-, B-, C- and D-type hydrogen bonds with oxygen atoms forming a wurtzite structure. The proton disorder is modelled within an eight-molecule supercell. Such a supercell has 17 symmetry inequivalent arrangements [15], (a four-molecule unit cell of this phase has only two unique symmetry arrangements $Cmc2_1$ and Cc). We chose particular supercells containing a representative selection of the possible orientations of molecules.

Ice Ic consists of a diamond lattice and only contains C- and or D-type hydrogen bonds. We use an eight-molecule supercell to model the proton disorder. In such a cell we found ninety configurations that obey the Bernal–Fowler rules, four of which are symmetry inequivalent. Here we use a cell containing a representative selection of the possible orientations of molecules. Ice Ic is a metastable phase and as such is not included on the phase diagram [13].

In moving across the water phase diagram (see figure 1) from ice Ih to ice VIII we observe progressive changes in the geometry of the ice phases. Ice IX and ice II have two conformations of the water molecule and ice II has two types of hexagonal rings, both consisting of 12 molecule unit cells. This 'pluralization' of the water molecules with increasing pressure stops with ice VI, which contains five different water molecule conformations in two very distorted sub-lattices. The ice VI structure used in the calculations is proton-ordered and contains ten molecules in the unit cell. This phase, however, has *average* values of its H–$\hat{\text{O}}$–H and $\alpha$ angular measurements (see section 5) closer to the collinearly bonded phases than either

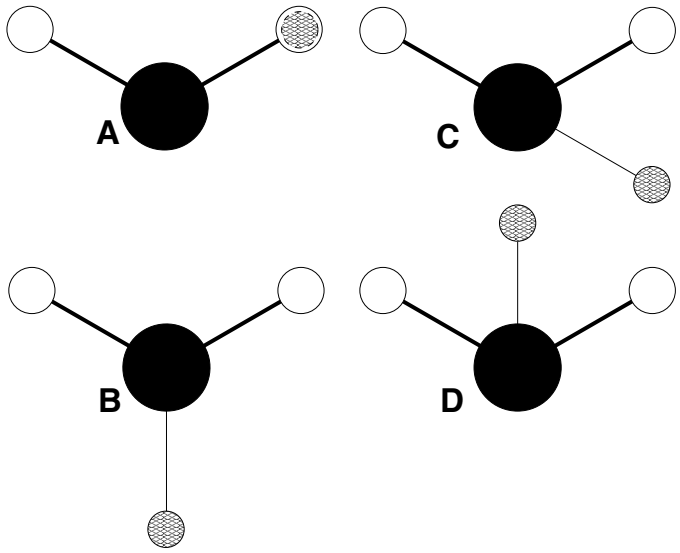


**Figure 2.** The geometrical arrangement of pairs of hydrogen bonded water molecules associated with the four different types of hydrogen bond possible in ice Ic, ice Ih, ice VII and ice VIII. The hydrogen bond is normal to the page and the atoms of the closest molecule represented by the large black circle (oxygen) and the smaller white circles (hydrogen). The covalent bonds of this molecule are represented by the thicker lines. The oxygen and one hydrogen atom of the other molecule involved in the hydrogen bond are masked. The remaining hydrogen of this molecule is represented by the small shaded circle with the thin line representing its covalent bond.

ice IX or ice II. Ice IX and ice VI are the only two phases in this study that do not possess hexagonal rings. These phases are neighbours with ice Ih and ice VIII, respectively. This suggests that these phases in particular possess structures with very compromised geometries (see section 5). For these structures the primitive unit cell is used in the calculations.

As the density of ice is further increased we reach the ice VII and VIII phases. Both of these structures consist of two inter-penetrating ice Ic hydrogen bonded lattices with non-hydrogen bonding interactions occurring between the sub-lattices. Ice VIII is a proton-ordered lattice with only D-type hydrogen bonds present. This results in sub-lattices with equal and opposite dipole moments. Ice VII is the proton-disordered version of ice VIII. We model the effect of proton disordering within 16 molecule supercells containing C- and D-type hydrogen bonds. Only structures with zero net dipole moments are considered. We chose to model ice VIII within a sixteen-molecule supercell for direct comparison with ice VII.

## 3. Computational methods

The electronic properties of the system are described using the *ab initio* pseudopotential method as implemented in the CASTEP code [16]. Here Kohn–Sham electronic states are described using a plane-wave basis set and conjugate-gradient minimization used to find the electronic ground state of the system. A norm-conserving pseudopotential is used to describe the oxygen core and a bare Coulomb potential to describe the proton. The kinetic energy cut-off of the plane-wave basis set used is relatively high (800 eV) in order to ensure convergence of electronic properties. The generalized gradient approximation (GGA) [17] to density-functional theory is used. This level of approximation has been shown to give a

good description [18] of the properties of hydrogen bonds central to this study. Because of the relatively large size of unit cells under study Γ point sampling of the Brillouin zone was used in each system. For uniqueness in each case the total energy was minimized with respect to all structural parameters including atomic positions and lattice vectors. No symmetry constraints were imposed on the lattice relaxation. Atomic positions were relaxed until the largest atomic force was less than 0.001 eV $A^{-1}$ and lattice vectors to 0.1%. Starting structures corresponding to oxygen atoms at symmetry sites and hydrogen positions determined by the isolated molecular structure were used. *Ad hoc* tests were performed with random shifts in starting structures but no difference in the final configurations for the structures described here was found. The principle source of differences between calculated and experimental structural parameters is the GGA. Typically O–O separations are predicted as being 2% too large compared with the experiment. This difference is large compared to predicted structural parameters in strongly bonded systems (covalent or ionic) using the same approximations and is a consequence of the sensitivity of hydrogen bonds to many electron effects. This fundamental limitation of the accuracy of predictions is used to further justify the use of Γ-point sampling of the Brillouin zone in describing the charge density. For example, increasing the density of sampling by a factor of eight in ice Ic results in a decrease in the predicted O–O separation of 0.17% and does not represent a significant improvement in comparison with experiment.

The relaxation of lattice vectors means that the zero-pressure properties of the ice phases are being predicted and we note that all phases considered except ice Ih are metastable at this pressure. The reasons for performing calculations at zero pressure are twofold. Firstly, this is the most unique choice of pressure we can make to perform comparisons across the phases [14] and secondly, the most extensive neutron scattering studies of ice with which we make comparison were performed using the recovered technique, i.e. by quenching the pressurized sample in liquid nitrogen and then releasing the pressure [2]. After the pressure release the structure remains with lattice parameters relaxing to their ambient-pressure values. Differences between zero pressure and ambient (1 atmosphere) pressure are insignificant.

The dynamical properties of the lattices under consideration are modelled within the harmonic approximation. The zone-centre dynamical matrix associated with the supercells are obtained by a finite-difference method based on the evaluation of atomic forces when atoms are shifted from their equilibrium positions [19, 20]. The calculation of the dynamical matrix is formulated as follows. We may write the total energy of the lattice as a truncated Taylor expansion [21]:

$$E = E_0 + \frac{1}{2}\sum_{ij} A_{ij}u_i u_j + \frac{1}{6}\sum_{ijk} B_{ijk}u_i u_j u_k \tag{1}$$

where $E_0$ represents the equilibrium lattice energy and $u_i$ is a general coordinate of an ion within the super cell relative to the minimum energy configuration ($i$ labels both the ion and a particular Cartesian direction). $A_{ij}$ and $B_{ijk}$ are constant second- and third-order tensors, respectively. $A_{ij}$ describes the harmonic response of the lattice and is used to construct the dynamical matrix from

$$D_{ij} = \frac{1}{(m_i m_j)^{1/2}} A_{ij} \tag{2}$$

where the $m_i$ represent the ionic masses. Note that the $u_i$ represents a periodic distortion of the lattice from the equilibrium, hence $A_{ij}$ is directly related to the dynamical matrix rather than

the force-constant matrix. Ignoring higher order terms in the energy expansion the force on a general coordinate is obtained as

$$F_i = -\frac{\mathrm{d}E}{\mathrm{d}u_i} = -\sum_j A_{ij}u_j - \frac{1}{2}\sum_{jk} B_{ijk}u_j u_k. \tag{3}$$

We now independently shift each general coordinate by an amount $\pm\Delta$ and minimize the total energy with respect to electronic degrees of freedom in order to obtain forces on all the ions in this distorted configuration. If $F_i^{\pm\Delta m}$ represents the force on coordinate $i$ due to a change in coordinate $m$ of $\pm\Delta$ then

$$F_i^{\pm\Delta m} = \mp\Delta A_{im} - \tfrac{1}{2}\Delta^2 B_{imm}. \tag{4}$$

Taking differences of the $F_i^{\pm\Delta m}$ we now obtain

$$F_i^{-\Delta m} - F_i^{+\Delta m} = 2\Delta A_{im} \tag{5}$$

from which $A_{ij}$ and hence $D_{ij}$ are directly obtained. This shift in opposite directions ensures cancellation of any cubic terms of the expansion whilst the quartic terms are assumed small enough to ignore. The magnitude of $\Delta$ must be large enough to overcome errors in the forces due to the noise produced by grid errors and small enough to ensure that quartic terms can be ignored. The shift is chosen to be 0.1 Å in all cases [22]. The method results in the evaluation of both $A_{ij}$ and $A_{ji}$, the symmetry of the problem is such that we must have $A_{ij} = A_{ji}$. Due to the non-symmetrical bonding in the systems under consideration and the finite-difference approximation this equality is not exactly realized. This is corrected for by symmetrization of the matrix after its complete evaluation. In addition sum rules dictate that $\sum_i A_{ij} = 0$. Again this is not exactly realized but is corrected by the distribution of the error in the sum rule evenly between all elements in the matrix before symmetrization. Satisfying this sum rule is especially important for the correct evaluation of the zero-frequency modes, the pre-processing of the matrix simply enforces the evaluation of the zero-frequency modes and does not significantly affect any other frequency.

We also note here that this direct evaluation of the dynamical matrix will not reproduce TO–LO splitting. However, these effects are expected to be small ($\sim$10 cm$^{-1}$) [23] and will not affect the findings of this study in any significant way. Similarly, acoustic modes (except zone edge modes in some cases) are not reproduced hence no comparison of experimental spectra is made in the acoustic frequency range.

## 4. Results

### *4.1. Static results*

The principal structural parameters of the fully relaxed structures (in order of increasing density) of the phases of ice considered in this study are shown in table 1 together with the corresponding experimental values. For completeness we have also included the experimental data of ice III, ice IV and ice V, whose structural complexity was beyond the scope of this study. Since the calculations are performed at zero temperature and pressure we compare them with data at the lowest available temperature extrapolated to atmospheric pressure [14]. The reasons for this choice of pressure are in order to make direct comparison with the IINS on the recovered phases as explained in section 3. In the case of orientationally disordered structures, the cell dimensions and number of molecules in a unit cell quoted refer to the supercells used to represent the disorder. In disordered structures the space group refers to the structure with average H-site occupancy. The O–O nearest neighbour distances quoted in

**Table 1.** The calculated and experimental structural data for the phases of ice in this study. The cell dimensions and number of molecules in a unit cell refer to the actual cells used in calculation. In the cases of disordered systems these data refer to the supercell used to model the disorder. The calculated data are listed first in each case followed by the experimental data in brackets. The experimental data for ice III, IV and V have been included for completeness.

| Ice phase | Crystal system | Space group[b] | Cell dimensions[a] (pm, deg) | Number of molecules in a unit cell | Number of nearest neighbours | Distance of nearest neighbours (pm) | O–O–O angles (deg) | Hydrogen positions ordered? | Density (g cm$^{-3}$) |
|---|---|---|---|---|---|---|---|---|---|
| Ih | Hexagonal | $P6_3/mmc$[b] | $a = 441$; $b = 763$; $c = 720$ | 8 | 4 | 270 | 109.5–109.6 | No | 0.989 |
| | | | ($a = 450$; $c = 732$) | | | (275) | (109.3–109.6) | | (0.93) |
| Ic | Cubic | Fd3m | $a = 623$ | 8 | 4 | 270 | 109.4 | No | 0.989 |
| | | | ($a = 635$) | | | (275 at $-130^\circ$C) | (109.6) | | (0.94) |
| II | Rhombohedral | R $\bar{3}$ | $a = 770$; $\alpha = 113.1$ | 12 | 4 | 273–281 | 76.3–131.6 | Yes | 1.216 |
| | | | ($a = 778$; $\alpha = 113.1$) | | | (275–284) | (80–128) | | (1.18) |
| III | Tetragonal | $P4_12_12$ | | 12 | 4 | | | No | (1.15) |
| | | | ($a = 673$; $c = 683$) | | | (276–280) | (87–141) | | N/A |
| IV | Rhombohedral | R $\bar{3}$ c | | 16 | 4 | | | No | (1.27) |
| | | | ($a = 760$; $\alpha = 70.1$) | | | (279–292) | (87.7–127.8) | | N/A |
| V | Monoclinic | A2/a | ($a = 922$; $b = 754$ $c = 1035$; $\beta = 109.2$) | 28 | 4 | (276–287) | (84–128) | No | (1.24) N/A |
| VI | Tetragonal | $P4_2/nmc$[c] | $a = 625$; $c = 577$ | 10 | 4 | 275–282 | 75.4–129 | No | (1.33) |
| | | | ($a = 627$; $c = 579$) | | | (280–282) | (76–128) | | 1.328 |
| VII | Cubic | Pn3m | $a = 685$ | 16 | 8 | 295–298 | 109.8 | No | (1.56) |
| | | | ($a = 686$) | | | (295) | (109.5) | | 1.485 |
| VIII | Tetragonal | $I4_1amd$[d] | $a = 685$; $c = 705$ | 16 | 8 | 299 | 110.3 | Yes | (1.56) |
| | | | ($a = 678$; $c = 699$) | | | (295) | (109.3–109.5) | | 1.443 |
| IX | Tetragonal | $P4_12_12$ | $a = 677$; $c = 688$ | 12 | 4 | 272–275 | 95–134 | Yes | 1.138 |
| | | | ($a = 673$; $c = 683$) | | | (276–280) | (87–140) | | (1.16) |

[a] For experimental data, values given are at atmospheric pressure and $-163$ °C unless noted otherwise.
[b] Unit cell used in calculations is orthorhombic with eight molecules in the unit cell.
[c] Ice VI used in calculations is proton ordered with space group Pmmn at $-163$ °C.
[d] Apply a tetragonal distortion along the $c$-axis to $a = b = c = 686$ pm where this is the zero pressure $c$ parameter of ice VII.

table 1 for ice VII and ice VIII refer to molecules in the same sub-lattice, i.e. to molecules hydrogen bonded to each other. The full spectrum of O–O distances are presented in figure 3, which also includes the non-hydrogen bonded O–O distances in ice VII and VIII. The range of O–O distances associated with hydrogen bonds are indicated between the arrows for ice VII and VIII. The geometry of the structures evolves from the low-density phases (ice Ic, ice Ih) through intermediate density (ice IX, ice II, ice VI) to the high-density phases (ice VII, ice VIII) with the spread of the geometrical data being dependent on the complexity of the

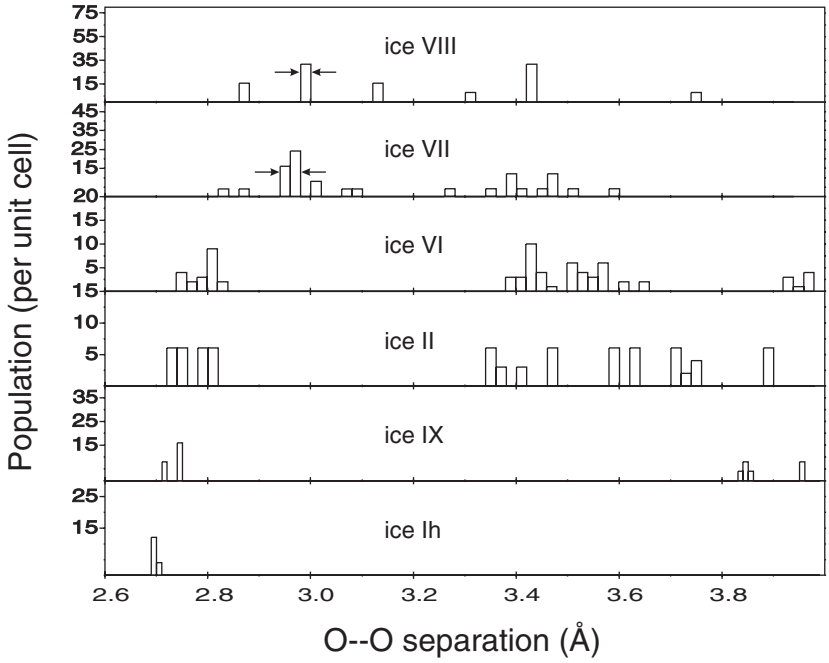


**Figure 3.** The calculated O–O separation data. For ice Ih, ice IX, ice II and ice VI all O–O separations below 2.9 Å correspond to hydrogen bonded O–O separations, values greater than this for these phases correspond to non-hydrogen bonded O–O separations. In ice VII and ice VIII the hydrogen bonded O–O separations are marked with pairs of arrows.

structure. These changes are manifest in the nearest neighbour distances and O–O–O angles. The predicted nearest neighbour distances increase from 2.70 Å in ice Ih and Ic to 2.99 Å in ice VIII. At intermediate densities the complexity of structures is manifest in the range of nearest neighbour distances. Similar changes are seen in the predicted O–O–O angles with angles in ice Ih and Ic being very close to the ideal tetrahedral angle (109.47) the range of angles then increases about this value for the intermediate density phases until a value close to the ideal tetrahedral one is again obtained in ice VII and VIII.

The range of H–O–H angles of $H_2O$ molecules that form the structures is presented in figure 4. Again the complexity of the intermediate-density structures is evident from the increased range of H–O–H angles. Also, comparing the low-density tetrahedrally coordinated structure ice Ih with the high-pressure tetrahedrally coordinated structures ice VII and VIII we find values in ice Ih closer to the ideal tetrahedral angle of 109.47° compared to ice VII and VIII. This trend is due to the longer, and weaker, H-bonds in ice VII and VIII allowing more relaxation towards the isolated water molecule value of 104.52°.

Further analysis of the predicted geometries is done with respect to three more angular terms as shown in figure 5. The motivation here is to further classify changes in the local geometry as a function of density and to provide explanations of trends in the dynamical properties in terms of trends in these geometrical properties. The angles are defined as follows: The $\alpha$ angle is defined as the difference between the HOH angle of a particular molecule and the $O_d$–O–$O_d$ angle formed between the oxygen atom of that molecule and the two oxygen donor atoms ($O_d$) involved in hydrogen bonds with hydrogen atoms of that molecule. The $\beta$ angle represents the difference in orientation of the plane associated with

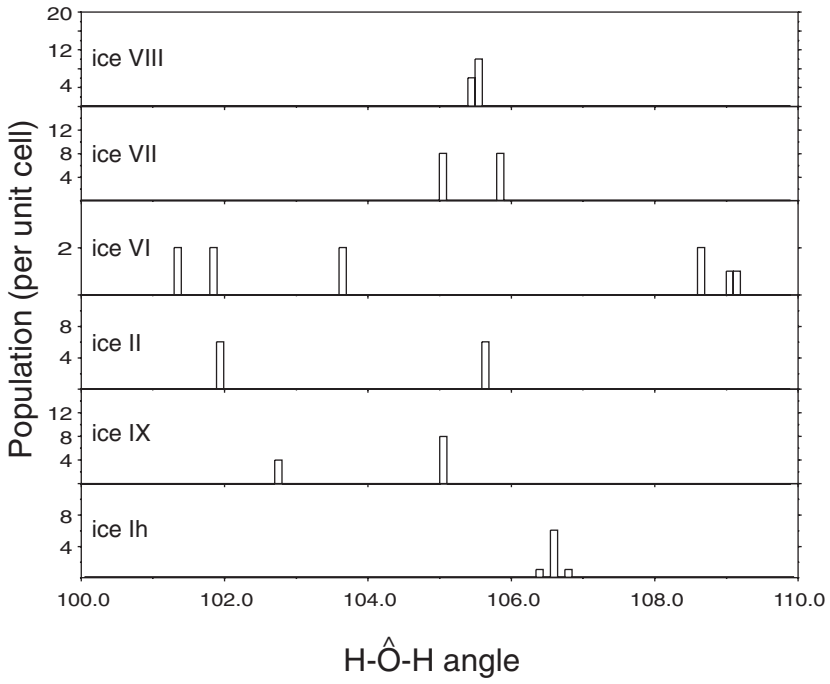


**Figure 4.** The calculated H–O–H angular data for ice Ih, ice IX, ice II, ice VI, ice VII and ice VIII. For reference the tetrahedral angle is 109.47° and the bond angle in the isolated water molecule is 104.52°.

a particular water molecule and the plane defined by the oxygen of that water molecule and the two $O_d$ atoms involved in hydrogen bonds to the hydrogen atoms of that molecule. The $\gamma$ angle is defined as the difference in orientation of the two planes defined by the hydrogen atoms of a particular molecule and the two $O_d$ atoms involved in hydrogen bonds with them, respectively. This angle represents the degree of twist experienced by a molecule relative to the associated $O_d$–O–$O_d$ plane.

The $\alpha$ angle data are presented in table 2 together with the corresponding values of $O_d$–O–$O_d$ and H–O–H angles. Phases with close to ideal tetrahedral coordination possess small positive values of the $\alpha$ angle and reflect the small difference between the ideal tetrahedral angle (109.47°) and the H–O–H angle of the isolated water molecule (104.52°). The distorted structures of ice IX and ice II phases have only negative values. In ice VI there are positive as well as negative values of the $\alpha$ angle and an average value of 3.2°, close to that of the collinearly coordinated phases. The $\beta$-angle data are presented in figure 6. Very small values of $\beta$ are predicted for the low- and high-density tetrahedrally coordinated phases of ice Ih, VII and VIII as expected on geometrical grounds and an increased range of values is seen for the intermediate density phases. Other features of note here are the large values of $\beta$ predicted in ice IX and VI. The $\gamma$-angle data are presented in figure 7. On geometrical grounds very small values of $\gamma$ are seen in the tetrahedrally coordinated phases. As structures are distorted away from the tetrahedral geometry $\gamma$ values with significant non-zero values are predicted. A feature of note is the symmetry of the $\gamma$ values in ice II about zero not present in the other intermediate density structures.

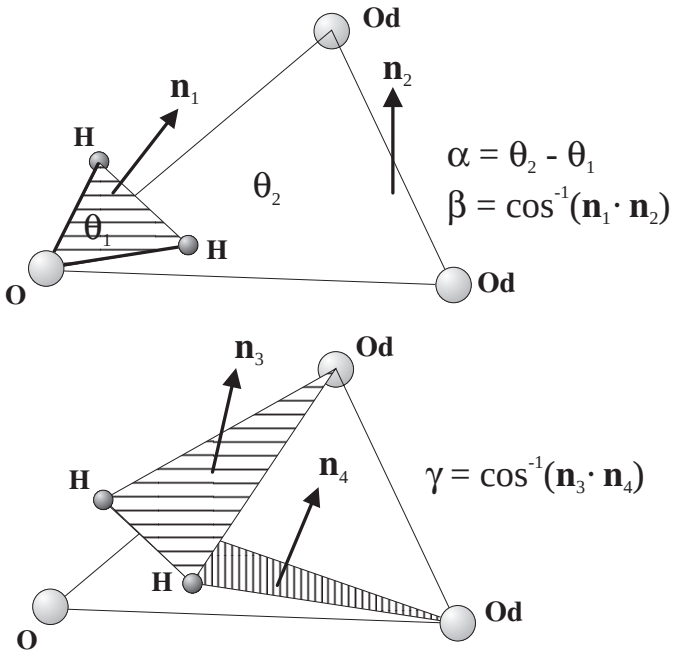


**Figure 5.** The geometry that defines the $\alpha$, $\beta$ and $\gamma$ angles referred to in the text. Large shaded spheres represent oxygen atoms and small shaded spheres hydrogen atoms. The oxygen to the lower left is covalently bonded to the two hydrogen atoms to form a particular molecule. The other two oxygens in the figure are the oxygen donors ($O_d$) involved in hydrogen bonds to the hydrogen atoms. $\theta_1$ is the H–O–H angle and $\theta_2$ the $O_d$–O–$O_d$ angle. $\mathbf{n}_1$ is normal to the H–O–H plane and $\mathbf{n}_2$ is normal to the $O_d$–O–$O_d$ plane. $\mathbf{n}_3$ and $\mathbf{n}_4$ are normals to the two H–$O_d$–H planes.

Other geometrical features of note are associated with the high-density ice VII and VIII phases. The presence of non-hydrogen bonded oxygen–oxygen separations in ice VII and ice VIII which are shorter than the hydrogen bonded oxygen–oxygen separations are clearly seen in figure 3. For ice VIII another structural parameter of interest is the relative displacement of one hydrogen bonded sub-lattice with respect to the other. Neither of the sub-lattices in ice VIII is centred in the interstices of its companion. The oxygens in one sub-lattice are displaced along the *c*-axis, a distance $\delta$ relative to the centred position. The value for $\delta$ as determined in this study for ice VIII is 0.23 Å. This compares well with the result of Ojamäe *et al* [11], which is 0.24 Å. Because of this displacement, each molecule has two non-hydrogen-bonded O–O separations (2.86 Å) which are closer than the four hydrogen-bonded O–O separations (2.99 Å). We conclude this section with a note that variations in O–O distances and $O_d$–O–$O_d$ angles associated with the disorder in ice Ih and Ic [13] are not well reproduced here, e.g. in ice Ic the $O_d$–O–$O_d$ angle is very close to the tetrahedral value, the origin of this disagreement is possibly related to the limited size of supercells used in the calculations. A related study by Nelmes *et al* [23] predicts significant distortion of sublattices in ice VII away from the ideal tetrahedral coordination. Further, we note here that none of the structural parameters presented here predict such a significant distortion in the sub-lattices. Again, the differences are attributed to the limited size of the supercell used to model the orientational disorder.

**Table 2.** The calculated angular data. Here H–O–H refers to a particular $H_2O$ molecule and $O_d$ refers to oxygen donor atoms involved in hydrogen bonds with the hydrogen atoms of that molecule. The $\alpha$ angle is given by ($O_d$–O–$O_d$)–(H–O–H) as defined in figure 5.

| Ice phase | $O_d$–O–$O_d$ angle (deg) | H–O–H angle (deg) | $\alpha$ angle (deg) |
|---|---|---|---|
| Ice Ic | 109.46 | 106.52 | 2.94 |
| Ice IX | 94.36 | 102.77 | −8.41 |
| | 96.00 | 105.03 | −9.03 |
| | 96.78 | 105.03 | −8.25 |
| Ice II | 85.48 | 105.64 | −20.16 |
| | 96.44 | 105.63 | −9.20 |
| | 85.48 | 101.97 | −16.49 |
| | 96.44 | 105.64 | −9.20 |
| Ice VI | 75.57 | 101.81 | −26.24 |
| | 90.80 | 103.68 | −12.88 |
| | 128.00 | 108.30 | 19.70 |
| | 126.04 | 108.61 | 17.43 |
| | 127.00 | 109.12 | 17.88 |
| Ice VII | 106.15 | 105.01 | 1.14 |
| | 108.14 | 105.82 | 2.32 |
| Ice VIII | 107.90 | 105.51 | 2.39 |

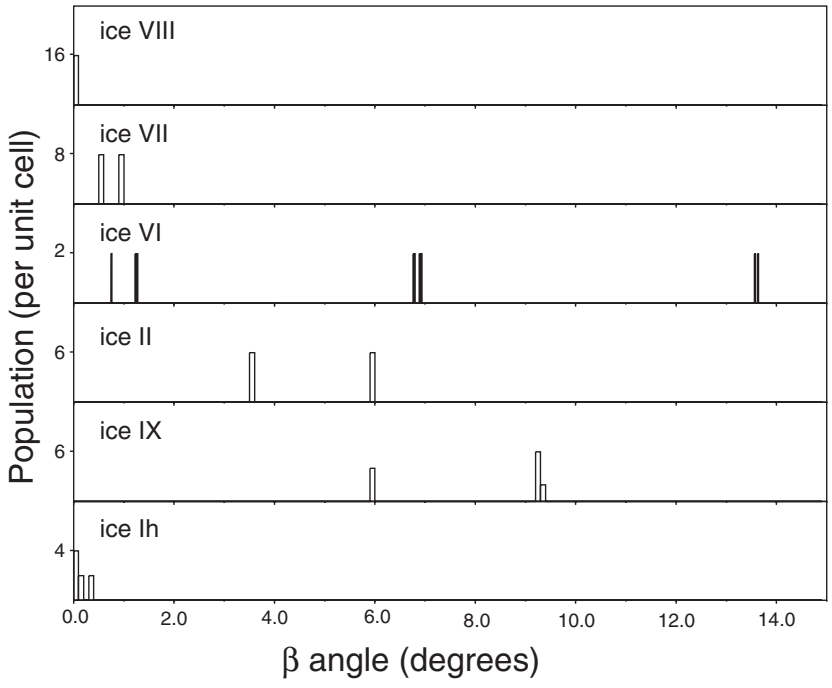


**Figure 6.** The calculated $\beta$ angle data for ice Ih, ice IX, ice II, ice VI, ice VII and ice VIII.

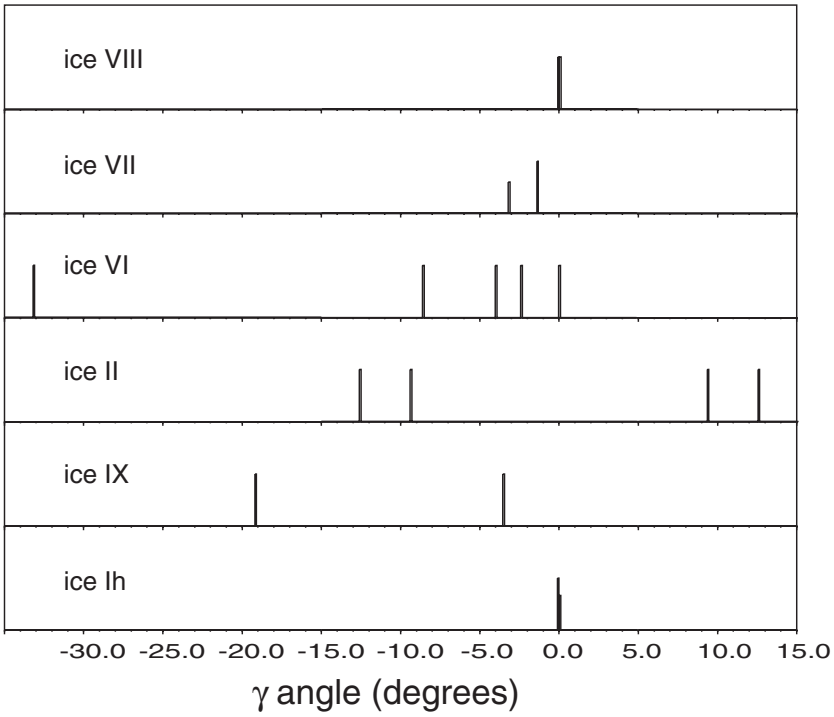


**Figure 7.** The calculated $\gamma$ angle data for ice Ih, ice IX, ice II, ice VI, ice VII and ice VIII.

### *4.2. Dynamic results*

The results of the dynamical calculations are presented in figures 8 and 9. The results are presented in the form of total density of states (DOS) and projected density of states (PDOS), where the DOS is projected onto intra-molecular modes of the isolated water molecule and rigid molecule inter-molecular modes. DOS are calculated from frequencies according to the expression

$$\rho(\omega) = \sum_j \partial(\omega - \omega_j)$$

and PDOS are calculated from the normal mode eigenvectors and frequencies using the expression

$$\rho_i(\omega) = \sum_j \sum_\tau \left(\underline{\nu}_\tau^i \cdot \underline{\nu}_j\right)^2 \partial(\omega - \omega_j)$$

where $\underline{\nu}_j$ is the set of normal mode eigenvectors resulting from the diagonalization of the dynamical matrix and $\omega_j$ the corresponding frequencies, $\omega$ is the frequency and $\partial(\omega - \omega_j)$ is a Gaussian broadening function used to obtain a continuous spectrum from the discrete set of frequencies. $\tau$ refers to a particular molecule in the unit cell and $\underline{\nu}_\tau^i$ represents 'pure' eigenvectors associated with individual molecules. The particular 'pure' molecular eigenvectors are the anti-symmetric stretch, symmetric stretch and bending normal-mode eigenvectors of each molecule together with eigenvectors representing rigid-molecule translations in the three Cartesian directions and rigid-molecule rotations about three perpendicular axes through the centre of mass of each molecule. The axes of rotation

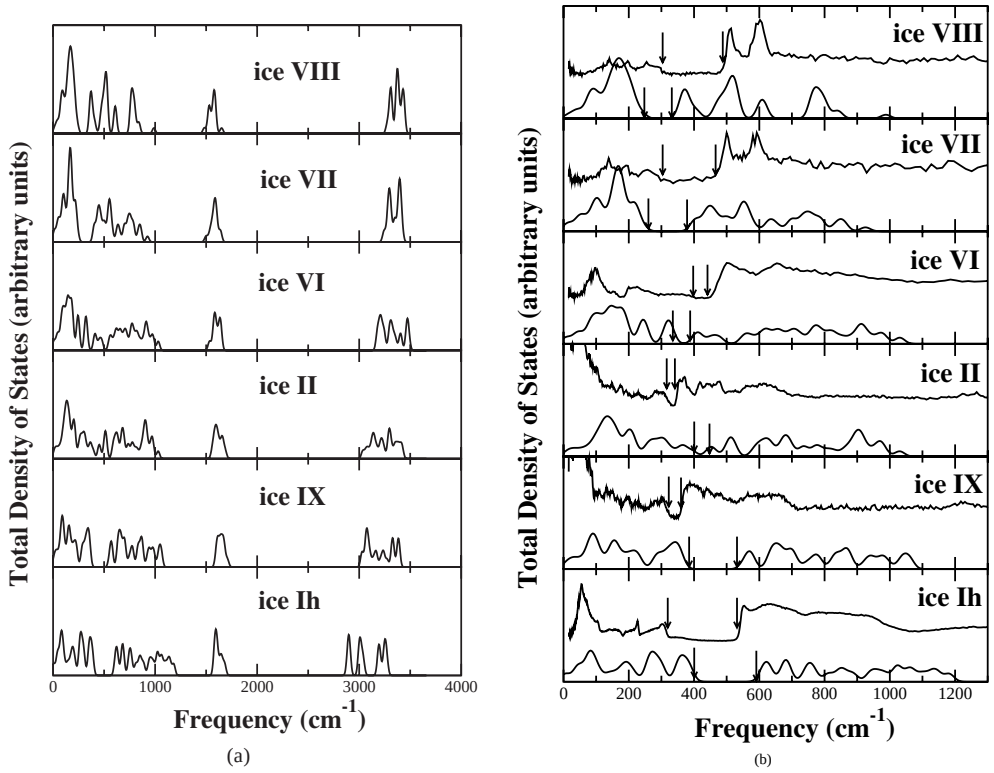


**Figure 8.** (a) The total density of states of all ice structures investigated here across the whole frequency range. (b) The calculated total density of states (lower curves) of all structures in the frequency range corresponding to molecular translation and rotation. For comparison the experimental neutron spectra [2] (upper curves) are included. The approximate upper edge of the translational band and lower edge of the rotational band are indicated by vertical arrows in each case for the purpose of comparison.

are denoted *x*, *y* and *z*, where the *y*-axis coincides with the $C_v$ symmetry axis of the molecule, the *z*-axis is perpendicular to the plane of the molecule and the *x*-axis is defined perpendicular to both of the other axes. The half width half maximum of the Gaussian broadening function used is 15 $cm^{-1}$ because this value is chosen as optimal in retaining the essential features of the frequency spectra. Because of the limited size of the supercells this represents an extremely coarse sampling of reciprocal space. The important features of the spectra are still clear, however, and comparison with the experimental spectra is still possible. The PDOS enable a clear understanding of the vibrational spectra in terms of molecular and lattice geometry.

The DOS across the whole frequency range of all phases studied is presented in figure 8(a). In all cases four distinct bands corresponding to intra-molecular stretch and bend and inter-molecular rotation and translation are observed. A magnification of the inter-molecular frequency range up to 1300 $cm^{-1}$ is presented in figure 8(b). The experimental IINS spectra [2] are also included in this figure for direct comparison. Indicated on this figure are the upper edge of the translational band and the lower edge of the rotational band for both theory and experiment. As previously mentioned for ice Ih, the predicted band edges can differ by as much as 100 $cm^{-1}$. Compared to the experiment, this is typical of frequencies calculated within current approximations used in density functional theory. However, features within bands are well reproduced in most cases.

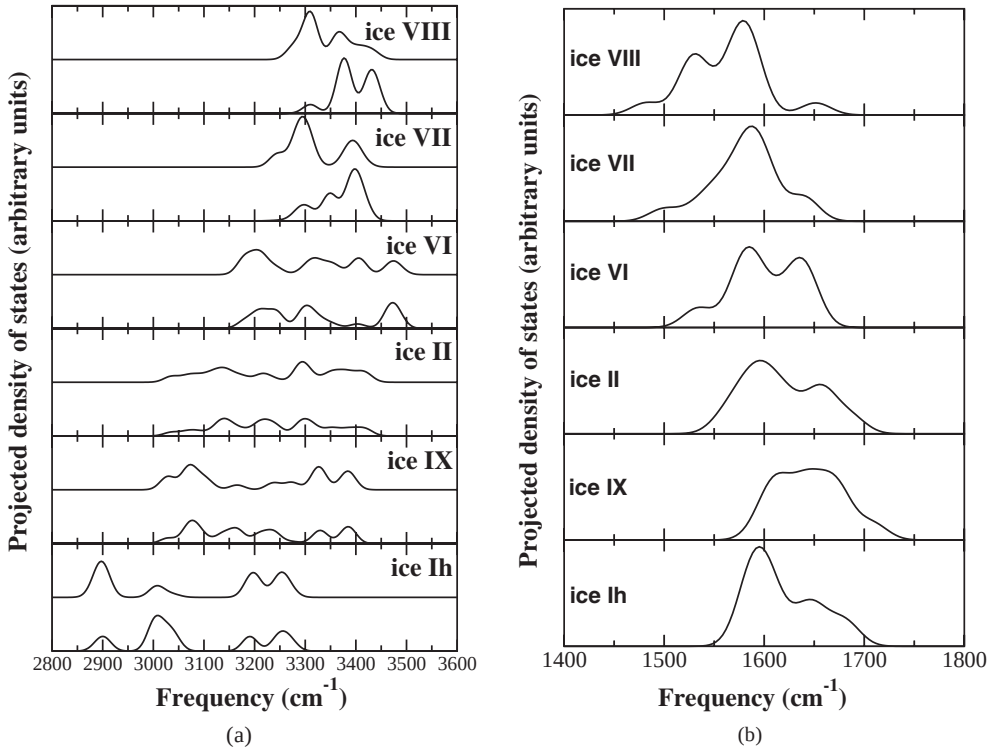


**Figure 9.** (a) The projections of the vibrational density of states onto the stretching motion of the isolated water molecule. For each phase the uppermost curve corresponds to the symmetric stretch component and the bottom one to the anti-symmetric stretch. (b) The projections of the vibrational density of states onto the bending motion of the isolated water molecule. (c) The projections of the vibrational density of states onto the rigid body rotational motion of the isolated water molecule. For each phase the *x*, *y* and *z* components of rotation are represented by the top, middle and bottom curves, respectively. (d) The projections of the vibrational density of states onto a rigid molecule translation relative to the Cartesian *x*, *y* and *z* axes. For each phase the *x*, *y* and *z* translational motions are represented by the top, middle and bottom curves, respectively.

As mentioned, the highest frequency band originates from the stretching modes of the isolated water molecule broadened by interactions with the hydrogen-bonded lattice. The PDOS associated with the projection onto the anti-symmetric and symmetric stretch normal mode eigenvectors of the isolated molecule are displayed in figure 9(a) in the frequency range 2750–3550 $cm^{-1}$. The PDOS associated with the bending normal mode eigenvector of the isolated molecule is displayed in figure 9(b) in the frequency range 1400–1800 $cm^{-1}$. The PDOS resulting from projection onto a rigid molecule rotational modes is displayed in figure 9(c) in the frequency range 300–1200 $cm^{-1}$. Finally, the PDOS resulting from projection onto a rigid molecule is displayed in figure 9(d) in the frequency range 0–500 $cm^{-1}$. For the frequency windows chosen associated with each distinct projection no observable PDOS lies outside the window on the same scale. Table 3 contains a summary of these regions, along with tabulated experimental data [2–5] for comparison. Again, as the calculations are performed at zero temperature and atmospheric pressure (the unit cell in each case was relaxed to the minimum-energy configuration) the experimental comparison is made to the lowest temperature results available with extrapolations to atmospheric pressure. There are no significant differences in the calculated

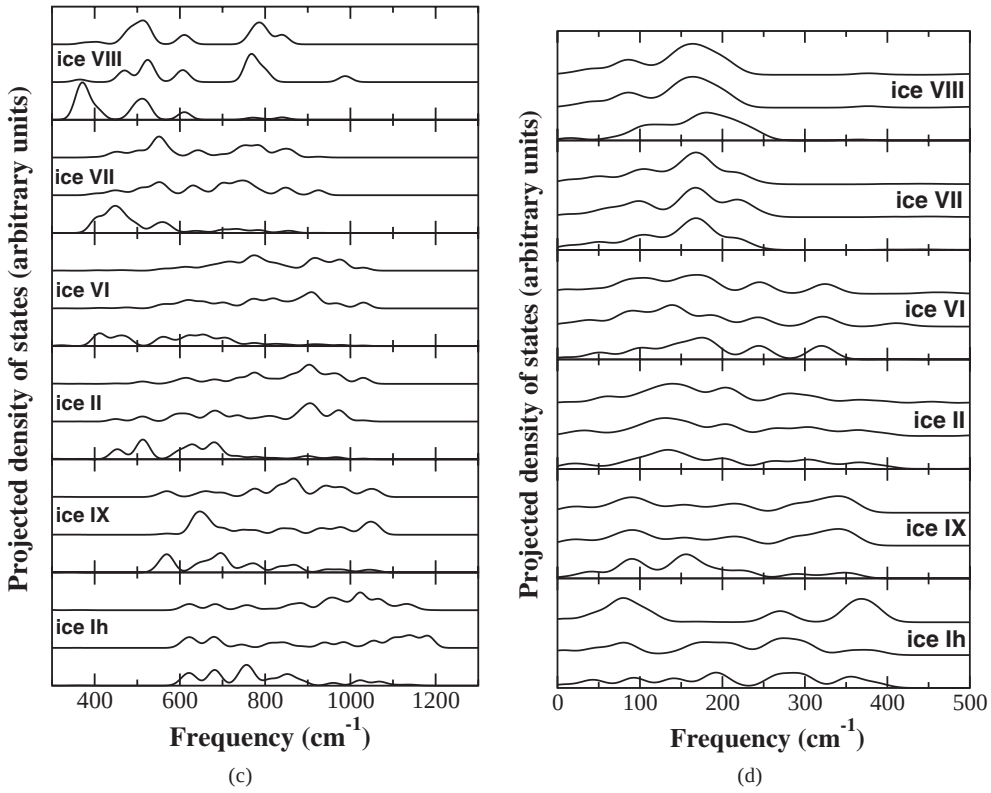


**Figure 9.** (*Continued*)

PDOS between the four possible proton orderings of an eight molecule ice Ic unit cell, or between the six (out of a possible 17 [15]) proton orderings of the ice Ih unit cell. As the PDOS for ice Ic and ice Ih are very similar we choose only to display them for ice Ih.

For phases possessing sub-lattices (ice VI, VII and VIII) we also performed projections onto rigid sub-lattice normal mode eigenvectors, here the 'pure' eigenvectors are translational modes where the rigid sub-lattices move relative to each other in the translational sense. Three independent translations are possible corresponding to relative motion of sub-lattices in the three Cartesian directions. The PDOS corresponding to projections onto these eigenvectors are shown in figure 10. In each case the PDOS is dominated by three particular normal mode frequencies. The frequencies of these three modes together with the corresponding direction of sub-lattice relative motion of the modes are shown in table 4. In table 4 we also list the magnitudes of the sum of the molecular dipole moments over each individual sub-lattice in the structures (denoted by SDM) in units of the individual molecular dipole moment $\mu$. The sum of the molecular dipole moments over the entire unit cell is denoted by TDM. A sub-lattice containing $N$ water molecules whose $C_v$ axes are all parallel to one another will have an SDM of $N\mu$. Also listed is **P,** the unit vector along the direction of the SDM for each sub-lattice, respectively. Note that the **P** of one sub-lattice is opposite to that of the other resulting in unit cells of zero total dipole moment. The character of these modes is determined by the non-hydrogen bonded interactions that exist between the sub-lattices [25].

An additional analysis was performed in the sub-lattice structures by repeating the PDOS analysis after the removal of sub-lattice interactions. This was done by setting to zero the

**Table 3.** Calculated and experimental frequency bands of the vibrational spectra for ice Ic, ice Ih, ice IX, ice II, ice VI, ice VII and ice VIII. The experimental results are taken from [2, 13, 14] and are included in brackets after the corresponding calculated values. For reference, the normal modes of vibration of the isolated water molecule are 3799 (3756) $cm^{-1}$ for anti-symmetric stretch, 3676 (3657) $cm^{-1}$ for symmetric stretch and 1595 (1505) $cm^{-1}$ for the bending motion. The experimental values are given in brackets.

| Ice phase | Translational band ($cm^{-1}$) | Rotational band ($cm^{-1}$) | Bending band[c] ($cm^{-1}$) | Stretching band ($cm^{-1}$) |
|---|---|---|---|---|
| Ice Ic | <394 | 580–1143 | 1540–1644, 1580 | 2837–3175 |
| Ice Ih | <385 | 610–1182 | 1584–1681, 1600 | 2888–3271 |
| | | (563–1006) | (1304–1755), (1610) | (3019–3462) |
| Ice IX | <359 | 553–1060 | 1599–1708, 1658 | 3027–3388 |
| | | (523–926) | (1369–1771), (1691) | (3035–3502) |
| Ice II | <394 | 448–980 | 1561–1687, 1590 | 3035–3422 |
| | | (499–886) | (1489–1787), (1707) | (3059–3518) |
| Ice VI | <329 | 405–1031 | 1534–1643, 1572 | 3178–3485 |
| | | (467–942) | (1530–1731), (1626) | (3140–3542) |
| Ice VII(A)[a] | <243 | 399–925 | 1499–1640, 1588 | 3241–3422 |
| Ice VII(B)[b] | <272 | 387–904 | 1532–1664, 1572 | 3242–3425 |
| Ice VIII | <241 | 365–988 | 1482–1652, 1580 | 3273–3437 |
| | | (451–966) | | |

[a] Both ice VII(A) and ice VII(B) consist of identical ice Ic sub-lattices anti-parallel to one another, where ice VII(A) consists of six C-and two D-type hydrogen bonds, respectively.
[b] Ice VII(B) consists of four C- and four D-type hydrogen bonds, respectively.
[c] The third frequency in every row represents the position of the peak in the bending band.

appropriate elements of the dynamical matrix before it was diagonalized. The motivation here was to quantify what effect the inter-sub-lattice interactions have on the vibrational density of states, in particular whether they significantly affect the difference in the positions of the top of the translational band of ice VIII (240 $cm^{-1}$) compared to ice Ih (394 $cm^{-1}$). This 'artificial' separation does not result in any significant shifts of the top of the translational band. For the high-pressure phases (ice VII and ice VIII) this drop is on average 7 $cm^{-1}$ and for ice VI it is 2 $cm^{-1}$. These small shifts suggest, although not conclusively, that the reduction in frequency of the upper edge of the translational band in going from ice Ih to ice VIII is principally due to the elongation and subsequent softening of the hydrogen bonds. This result also suggests that the inter-sub-lattice interactions do not significantly affect the chemical nature of the hydrogen bonds.

## 5. Discussion

Each region of the spectrum obtained using the methods outlined above has structure that reflects the geometrical characteristics and environments of the molecules making up the different phases. Here we discuss trends in the dynamical results with respect to changes in the complexity of the molecular environments.

### *5.1. The stretching region*

Here we discuss a series of observations about the PDOS corresponding to the stretching region and trends in the changes observed across the phase diagram. In particular we discuss

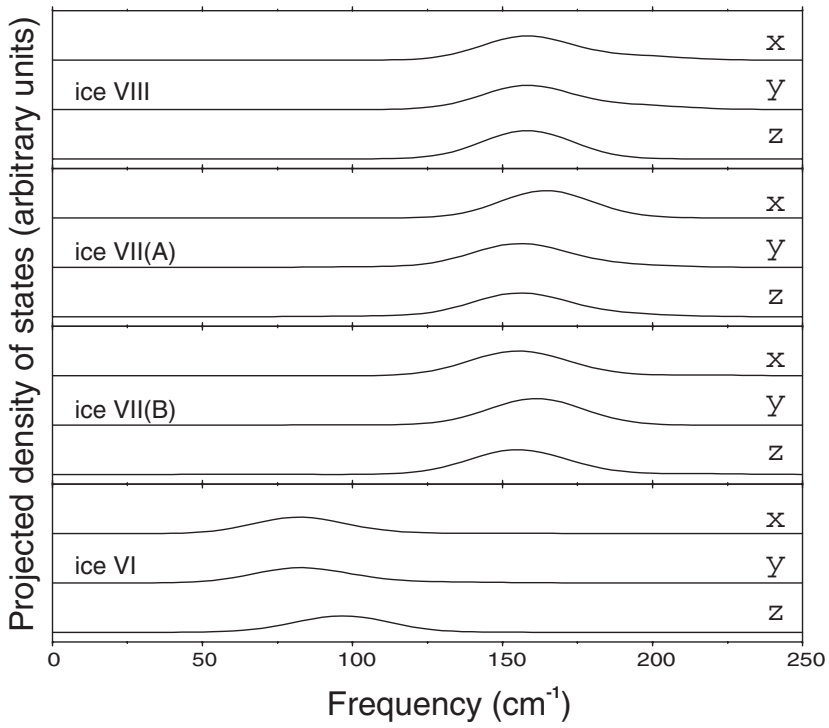


**Figure 10.** The projection of the vibrational density of states onto rigid sub-lattice motion. The sub-lattice motion is analysed by calculating a difference vector of the rigid body centre-of-mass motions of the two sub-lattices, then projecting the components along each of the three crystallographic directions.

the structural factors, which determine the width of each band and the positions of the upper and lower edges of the bands.

In an isolated water molecule the normal modes with the highest frequencies are the anti-symmetric stretch mode (3756 $cm^{-1}$) and the symmetric stretch mode (3657 $cm^{-1}$). When the molecule is introduced into the lattice it will interact with other water molecules via the hydrogen bond network. This interaction results in coupling of the anti-symmetric and symmetric stretch motions (except where symmetry forbids coupling in certain systems). In general, increased coupling of the water molecules to the hydrogen bond network will lower the frequency of the associated normal modes and broaden them into bands.

Starting with the highest density structures, ice VIII and VII, we observe bands with the smallest widths and starting at the highest frequencies of all structures considered. This is indicative of the longer O–O distances in these structures resulting in the elongation and subsequent weakening of the hydrogen bonds. There is considerable overlap of the symmetric stretch band and anti-symmetric stretch band in these structures, although it is still clear that anti-symmetric stretch-type motion is associated with a higher frequency compared to symmetric stretch-type motion as it is in the isolated water molecule. As the density of the structures decreases we observe considerable broadening of the bands and lowering of the bottom edge of the bands in ice VI, ice II and ice IX. The latter is due to, and elaborated on below, the shorter stronger hydrogen bonds present in these structures. The broadening is due to considerable increase in complexity of the structures resulting in a wide range of

**Table 4.** The frequencies of the dominant modes in projections onto rigid sublattice motion together with features relating to the geometry of the particular structures. The quantities defined here are described in detail in section 4.2. Although the two sub-lattices interact with one another they are not 'bonded' together in the same way as the hydrogen bonds bond the water molecules since the total energy of the ice VIII structure is not stationary with respect to the two sub-lattices.

| Ice phase | $\omega$ ($cm^{-1}$) | **r** | SDM | TDM | **P** |
|---|---|---|---|---|---|
| Ice VIII | 158.4 | −0.300, 0.172, −0.938 | | | 0.00, 0.00, 1.00 |
| ↑↓ | 158.2 | 0.303, 0.949, 0.090 | 8.000 | 0.000 | |
| | 158.1 | −0.888, 0.247, 0.388 | | | 0.00, 0.00, −1.00 |
| Ice VII(A)[a] | 163.0 | −0.001, −1.000, 0.000 | | | 0.00, 1.00, 0.00 |
| ↑↓ | 150.0 | −0.573, 0.000, −0.819 | 4.000 | 0.000 | |
| | 149.2 | −0.820, 0.000, 0.573 | | | 0.00, −1.00, 0.00 |
| Ice VII(B) | 164.1 | 1.000, 0.000, 0.000 | | | 0.00, $1/2^{1/2}$, $-1/2^{1/2}$ |
| ↑↓ | 160.6 | 0.004, 0.704, 0.710 | $(32)^{1/2}$ | 0.000 | |
| | 150.7 | 0.000, 0.701, 0.713 | | | 0.00, $-1/2^{1/2}$, $1/2^{1/2}$ |
| Ice VI | 97.7 | −0.088, 0.309, 0.947 | | | 0.46, 0.43, 0.78 |
| ↑↓ | 82.3 | −0.832, −0.531, 0.117 | 4.247 | 0.000 | |
| | 80.7 | −0.539, 0.776, −0.326 | | | −0.46, −0.43, −0.78 |

[a] Structures consisting of the same sub-lattices as A but with the *c*-axes of their sub-lattices positioned parallel or at right angles to one another are found to be unstable, since both of these arrangements have non-zero total molecular dipole moment. The arrangement with parallel sub-lattices has a total molecular dipole moment of 8 and the unit cell composed of orthogonal sub-lattices has a total molecular dipole moment of $(32)^{1/2}$.

hydrogen bond lengths and strengths and a range of coupling to the hydrogen bond network due to geometrical factors as described later. These trends are also observed in the neutron spectra (see figure 18 of [2] and table 3).

In general, the extent to which a particular water molecule will couple with the rest of the lattice (and hence have the frequency of its normal modes lowered) will depend on two factors: the length of the hydrogen bonds separating it from the rest of the lattice and the degree of non-collinearity of the covalent bonds and hydrogen bonds originating from each hydrogen atom. This latter condition appears to be more powerful as demonstrated by the fact that ice VI has the highest stretching frequency of all the phases at 3485 $cm^{-1}$, i.e. the closest value to that obtained for the isolated water molecule. Again, the trends here are in agreement with the neutron scattering spectra. Examination of the $\alpha$ and $\beta$ angles (see table 2 and figure 6) shows ice VI has the least collinear covalent and hydrogen bonds of all the phases in this study, although its hydrogen bonds are shorter (1.80–1.86 Å) than those in ice VIII (2.01 Å). The geometrical effect here is due to the fact that for a collinear structure the covalent bond stretch will maximally couple to the hydrogen bond (i.e., induce maximal changes in its length) compared to a non-collinear arrangement (in a structure where the covalent bond and hydrogen bond are perpendicular, to a first approximation, a change in the covalent bond length due to a molecular stretch will induce no change in the hydrogen bond length).

If we consider a normal mode eigenvector where the characteristic motion associated with each molecule is dominated by either symmetric stretch-type motion or anti-symmetric stretch-type motion, then the relative phase of the motion on adjacent molecules plays a role in determining the frequency [26, 27]. For a pair of molecules bonded by a collinear hydrogen bond the relative phase of anti-symmetric stretch-type motion has minimal effect. Here the

motion of the hydrogen bonded oxygen is perpendicular to the hydrogen bond and does not play a role in the distortion of the hydrogen bond and the associated coupling, i.e. in an anti-symmetric stretch mode of an isolated molecule the oxygen moves perpendicular to the axis of symmetry. Conversely, if both molecules involved in the hydrogen are undergoing symmetric stretch-type motion then the direction of motion of the hydrogen bonded oxygen is parallel to the hydrogen bond, i.e. in a symmetric stretch mode of an isolated molecule the direction of motion of the oxygen is along the axis of symmetry. In this case if both molecules move in phase there is maximal distortion of the hydrogen bond and maximal coupling and if both molecules move out of phase there is minimal distortion of the hydrogen bond and minimal coupling. It is this behaviour that causes the highest and lowest frequencies in the stretching bands of ice Ic and ice Ih to have symmetric stretch character. Similar couplings exist between mixed symmetric stretch and anti-symmetric stretch modes and result in a distinct splitting of the stretching bands in ice Ic and ice Ih into bands of in-phase and out-of-phase character. This splitting is also in agreement with the neutron spectra of [2] where evidence of two distinct bands in this region is seen. The splitting is not complete as predicted here due to instrument resolution resulting in a broadening of the features.

The top halves of the stretching bands in ice VI, ice VII and ice VIII are mainly anti-symmetric stretch. In these structures the phase splitting outlined above is smaller than the difference between anti-symmetric and symmetric stretch frequencies. Ice VII(A) (78%), ice VII(B) (76%), ice VIII (83%) and ice VI (61%) all possess a highest frequency mode whose projection is predominantly onto the anti-symmetric stretch motion. The percentage of anti-symmetric stretch is given here in brackets next to the appropriate structure. Conversely, for ice Ic and ice Ih the top half of the modes in the stretching band have more symmetric stretch character than anti-symmetric stretch character for the reasons explained above. The upper edge of the stretching region moves up in frequency with increasing density and the projection onto the anti-symmetric motion at this frequency increases. This is perhaps counter-intuitive but is due to the lengthening of hydrogen bonds with increasing density, as the open near-tetrahedrally coordinated structures are distorted into more close packed ones. The lower edge of the stretching region moves up in frequency with increasing density. For all of the phases the symmetric stretch projection extends to lower frequencies compared to the corresponding anti-symmetric stretch projection. This effect is most pronounced in ice Ic, closely followed by ice VII and ice VIII, and is rather less pronounced in ice IX, ice II and ice VI due to the very distorted structures preventing coupling of the covalent and hydrogen bonds as explained above.

### *5.2. The bending region*

Changes in the bending region as a function of structure are in general less dramatic than the changes seen in the stretching region. This is due to the fact that in structures with collinear bonds, to a first order of approximation, hydrogen bonds are not affected by bending distortions of molecules. In such distortions the motion of hydrogen atoms is perpendicular to the hydrogen bonds. The motion of the oxygen has a component along the hydrogen bond but this is small. The overall shift of the bending modes from the isolated molecule (frequency 1505 $cm^{-1}$) is much smaller than the stretching modes for this reason. The general downward trend in the lower edge of the bending band and the broadening of the band from ice Ih through to ice VIII is attributed to the increasing non-collinear nature of hydrogen bonds and subsequent increase in the coupling of bending normal modes to the lattice. In the sub-lattice structures (ice VI, VII and VIII) non-hydrogen bond interactions also play a role.

The $\beta$-angle data can be used to explain the relative positions of the upper edge of the bending band for all the described ice phases. We observe that the magnitude of the $\beta$ angle is linked with a tendency to rotate about the $x$-axis of a molecule, and so provides a measure of the resistance of a particular molecule to bending motions. This is illustrated for ice IX whose type I molecules are characterized by a particularly large $\beta$ angle. This explains why the frequencies of its entire bending band are higher than any other of the phases; out of step with its position on the phase diagram with a peak at 1658 $cm^{-1}$ (see table 3).

For all phases we have assigned the peak in the bending band as the particular frequency that has the maximum mixing of the $x$-component of rotation: this coincides with the largest intensity peak in each of the bands seen in the Gaussian broadened spectra. We observe that for every phase there is a bending mode which has at least an order of magnitude more rotational mixing than any other projection. It is always the $x$-component of rotation that is dominant at this frequency rather than the $y$- or $z$-component. For all phases, molecules with the largest projections onto the bending motion have the largest mixing with the symmetric-stretch projection and the smallest mixing with any of the rotational projections.

This behaviour is particularly clearly illustrated for ice IX; the type I molecules have contributions to the density of states for the peak in the bending projection an order of magnitude smaller than the contributions from the type II molecules. At the bending peak the type I molecules have no appreciable coupling with any rotational or translational motion, which would bring down the frequency. Type I molecules produced an overall mixing with the symmetric stretch projection that was three times greater than for the molecules in ice Ih whereas type II molecules did not possess any significant mixings with the stretching motions. Coupling to stretching motion raises the frequencies and so the combination of it and the lack of mixing with the rotational and translational motions explains why overall ice IX has such a high bending frequency. It is possible that the extreme geometry of ice IX has altered the chemical nature of the constituent covalent and hydrogen bonds. In fact it is shown in [25] that the hydrogen bonds in ice IX are partly covalent in character, more so than any of the other ice phases.

### *5.3. The rotational region*

The denser the phase is, the lower the rotational frequencies will be. Again, this counterintuitive fact is a consequence of the hydrogen bonded O–O distances lengthening with increasing density. The longer the hydrogen bonds the weaker they are and consequently, the lower the characteristic frequencies of lattice vibrations. Comparison with experimental spectra [2] in this region is again favourable. The overall decrease in frequency in this region is clearly observable. Again we note there is typically a 100 $cm^{-1}$ error in the position of the lower edge in the rotational spectra which we attribute to the GGA. Particular features of note reproduced in the spectra include the broad featureless spectra of ice Ih, the dominance of low frequency modes in ice IX, the prominent two peaks near the lower edge of the rotational band and the higher frequency peak at $\sim$800 $cm^{-1}$ in ice II and similar features in ice VI and the extremely prominent double peak at the lower edge in ice VIII. The ability to reproduce the rich variety of features in this region indicates that dispersion does not play an important role in determining the spectra.

For a particular phase we observe a connection between the $\alpha$, $\beta$ and $\gamma$ angles in the relaxed structure and the $z$-, $x$- and $y$-components of rotation, respectively. The larger the particular angle, the more dominant the corresponding type of rotation is at the bottom of the rotational band. We illustrate the connection between the range of the angular data in the relaxed structure and the $z$-, $x$- and $y$-components of rotation for ice IX and ice II where

they are particularly clear. At the bottom of the rotational band of ice IX the projections onto the $x$- and $z$-components of rotation for the type II molecules are an order of magnitude larger for those of the type I molecules. The type I molecules have the same order of magnitude of projections onto the $x$ and $y$ components of rotation whereas the type II molecules have negligible contributions from the $y$ components of rotation. The type I and type II molecules possess $\gamma$ angles of magnitudes $<3.5^\circ$ and $>19^\circ$, respectively, and the former more readily perform $y$-rotations since these molecules are more collinear with their connecting hydrogen. The type I molecules are more resistant to undergoing $x$-rotations at the bottom of the rotational band than are the type II molecules. This is evident by the type I molecules coupling to the bending motions at the bottom of the rotational band. Since they have large $\beta$ angles, no such mixings occur for the type II molecules. For ice II the $y$-component of rotation is greater than for any other phase at the bottom of the rotational band. Examining the ice II $\gamma$-angle data shows that this is the only phase for which there are two narrow bands of positive and negative $\gamma$ data having the same magnitude. So in ice II *both* hydrogen bonds attached to a water molecule can be twisted relative to it; this correlates with the ease of $y$-rotation. Ice VI has virtually no $x$- or $y$-rotation contributions at the lower edge of the band. This is due to the $\beta$ and the $\gamma$ angles having a broad range of values. We might expect the bottom of the rotational bands of ice Ic and ice VIII to be similar since both structures possess close to ideal tetrahedral coordination of the oxygen lattice. This is not the case. Ice Ic has negligible contributions from the $y$-component of rotation and non-negligible $x$-rotational contributions, the converse being true for ice VIII. The explanation for this difference may lie in the influence of the sub-lattices in ice VIII, evidenced by mixings with translational motion, in particular translational components parallel to the $c$-axis. Ice Ic has no translational components parallel to the $c$-axis.

### *5.4. Translational region*

The reproduction of features in the experimental spectra in this region is again favourable. As for the rotational region predicted frequencies differ by $\sim$100 cm$^{-1}$ compared to the experiment due to the approximate nature of the GGA. The computational method employed here is not capable of reproducing the acoustic region hence no attempt to compare features in this region is made. Features in the optical bands at the upper edge of the translational region are well reproduced. The double-peak structure observed experimentally in ice Ih in this region is clearly reproduced together with its contraction into a single peak in higher density structure with longest H-bonds. A complete description of the origin of this feature is subtle and will appear elsewhere [27].

The PDOS associated with translational motion of the water molecules is shown in figure 9(d). The higher pressure phases have the tops of their bands pushed down relative to those of the lower pressure phases mainly due to the lengthening hydrogen bonds rather than interactions between non-hydrogen bonded oxygens that exist between the sub-lattices. The lengthening hydrogen bonds allow freer motion of the water molecules so that they bind together. In ice VII(B) the top of the translational band calculated is about 30 cm$^{-1}$ higher than for either ice VII(A) or ice VIII. This could be explained by the fact that **P** (see section 4.2.) is influencing the optic-type motion at the top of the translational band. **P** has two non-zero components for ice VII(B) (see table 3) whereas for ice VII(A) and ice VIII **P** has only one component. This may explain why the frequencies at the top of the translational band for ice VII(A) and ice VIII are so similar. For ice VI the sub-lattices will interact less than for ice VIII or ice VII since the closest non-hydrogen bonded oxygens are separated by nearly 3.4 Å. Ice II does not have sub-lattices, but like ice VI, ice VII and ice VIII it does not have a

frequency gap between the top of the translational band and the bottom of the rotational band. This absence of a distinct gap in ice II is due to the proximity of the non-hydrogen bonded oxygens (less than 3.35 Å).

In structures possessing sub-lattices translational normal modes exist in which the rigid sub-lattices move relative to each other. The Raman spectrum of ice VIII for relative motion of the centres of mass of the two sub-lattices is available [28]. We compare these to the three calculated normal modes of ice VIII which behave in this way (see table 4). In the following section we always refer to the highest of the three frequencies given for each of the structures in table 2. The experimental frequency corresponding to the relative displacement of the two sub-lattices parallel to the $z$-axis (169.2 $cm^{-1}$) compares well with our calculated frequency (158.4 $cm^{-1}$). Note that in this mode there are non-negligible mixings of $x$- and $y$-translational components. This is due to the coupling of $x$- and $z$-components of rotation with the motion parallel to the $z$-axis. It was also found in [28] that the value of the isotope ratio (i.e. the $H_2O/D_2O$ frequency ratio) for this motion was 1.047. The authors attributed the difference between this value and the value of 1.054 (for harmonic translational motion, the ratio of the square root of the molecular masses, $(20/18)^{1/2}$) to the presence of coupling with stretching, bending or rotational motion. We obtain an isotope ratio of 1.041 for this normal mode in ice VIII. Inelastic incoherent neutron scattering data [29] give the closest peak with a frequency of 166.7 $cm^{-1}$ and isotope ratio as 1.045, which corresponds better to our data. For ice VII(A) and ice VII(B) we obtain isotope ratios of 1.045 and 1.048, respectively. These two values show that the rigid motion of the sub-lattices is more harmonic than for ice VIII (especially in the ice VII(B) case). This is clearly demonstrated for the **r** values in table 4.

## 6. Conclusions

We have been able to apply geometrical analysis to explain the important features of the vibrational density of states in each of the stretching, bending, rotational, translational and sub-lattice projections. It was important to perform the molecular projections outlined, rather than working with the total spectra especially for the disordered phases in order to describe links between the structure and vibrational frequencies in all the phases studied. Additional projection onto sub-lattice motion has allowed the non-hydrogen bonded interactions between sub-lattices to be probed. In a parallel study the chemistry of interactions in these molecular solids has been fully described using the theory of 'atoms in molecules' [25, 30].

## Acknowledgments

We are grateful to S R Kirk and D K Ross for careful reading of the manuscript. We are grateful for the financial support of the EPSRC in the form of a PhD studentship for SJ.

## References

[1] Whalley E 1969 *Physics of Ice* ed N Riehl (New York: Plenum) pp 19–43
Franks F*et al* 1973 *Water, A Comprehensive Treatise* vol 1 ed F Franks (New York: Plenum) ch 4
Whalley E 1976 *The Hydrogen Bond—Recent Developments in Theory and Experiments* vol 3 ed P Schuster *et al* (Amsterdam: North-Holland) ch 29 pp 1425–70
[2] Li J-C 1996 *J. Chem. Phys.* **105** 6733 (Note: data in this publication used in figure 8(b) are available in the ISIS INS database on the web at http://www.isis.rl.ac.uk/molecularSpectroscopy)
[3] Li J-C, Londono J D, Ross D K, Finney J L, Tomkinson J and Sherman W F 1991 *J. Chem. Phys.* **94** 6770
[4] Li J-C, Londono D, Ross D K, Finney J L, Bennington S M and Taylor A D 1992 *J. Phys.: Condens. Matter* **4** 2109

[5] Li J-C, Ross D K, Londono J D, Finney J L, Kolesnikov A and Ponyatovskii E G 1992 *Physics and Chemistry of Ice* ed N Maeno and T Hondoh (Sapporo: Hokkaido University Press) pp 43–9
[6] Bernal J D and Fowler R H 1933 *J. Chem. Phys.* **1** 515
[7] Heggie M I, Latham C D, Maynard S C P and Jones R 1996 *Chem. Phys. Lett* **249** 485
[8] Newton M D 1983 *Acta Crystallogr.* B **39** 104
[9] Knuts S, Ojamäe L and Hermansson K 1993 *J. Chem. Phys.* **99** 2917
[10] Cummings P L, Bacskay G B and Hush N S 1987 *Mol. Phys.* **61** 795
[11] Ojamäe L, Hermansson K, Dovesi R, Roetti C and Saunders V R 1994 *J. Chem. Phys.* **100** 2128
[12] Lee C and Vanderbilt D 1993 *Chem. Phys. Lett.* **210** 279
[13] Petrenko V F and Whitworth R W 1999 *Physics of Ice* (Oxford: Oxford University Press)
[14] Hobbs P V 1974 *Ice Physics* (Oxford: Clarendon)
[15] Howe R 1987 *J. Physique Coll.* C1 **48** 599
[16] Payne M C, Teter M P, Allan D C, Arias T A and Joannopoulos J D 1993 *Rev. Mod. Phys.* **64** 1045
[17] Perdew J P and Wang Y 1992 *Phys. Rev.* B **46** 12 947
[18] Hamann D R 1997 *Phys. Rev.* B **55** 10 157
[19] Morrison I, Jenkins S, Li J-C, Xantheas S S and Payne M C 1997 *J. Phys Chem.* B **101** 6146
[20] Ackland G J, Warren M C and Clark S J 1997 *J. Phys.: Condens. Matter.* **9** 7861
[21] Dolling G 1996 *Method. Comput. Phys.* **15** 1
[22] Jenkins S 1999 *PhD thesis* University of Salford
[23] Nelmes R J, Loveday J S, Marshall W G, Hamel G, Besson J M and Klotz S 1998 *Phys. Rev. Lett.* **81** 2719
[24] Klug D D, Tse J S and Whalley E 1991 *J. Chem. Phys.* **95** 7011
[25] Jenkins S and Morrison I 2000 *Chem. Phys. Lett.* **317** 97
[26] Morrison I and Jenkins S 1999 *Physica B: Phys. Condens. Matter* **263** 442
[27] Morrison I and Jenkins S to be published
[28] Wong P T T and Whalley E 1976 *J. Chem. Phys.* **64** 2359
[29] Kolesnikov A, Li J-C, Ross D K, Sinitzin V V, Barkalov O I, Bokhenkov E L and Ponyatovskii E G 1992 *Phys. Lett.* A **168** 308
[30] Jenkins S and Morrison I 1999 *J. Phys. Chem* **103** 11 041